# A study of friction microslip modelling for dynamic analysis of bladed discs with root joints

Article (Accepted Version)

Article type: Material Stress Analysis, Structures

Corresponding author: E.P. Petrov

University of Sussex, Brighton BN1 9QT, United Kingdom, e-mail: y.petrov@sussex.ac.uk

# A study of friction micro-slip modelling for dynamic analysis of bladed discs with root joints

Junjie Chen[1], Chaoping Zang[1], Biao Zhou[1], E.P. Petrov[2]

[1] Nanjing University of Aeronautics and Astronautics, Aero-engine Thermal Environment and Structure Key Laboratory of Ministry of Industry and Information Technology, Nanjing 210016, China, e-mails: chen_junjie@nuaa.edu.cn; c.zang@nuaa.edu.cn; biao.zhou@nuaa.edu.cn;
[2] University of Sussex, Brighton BN1 9QT, United Kingdom, e-mail: y.petrov@sussex.ac.uk

## Abstract

In the machinery structures with joints the contact pressures at contact interfaces are usually high enough to ensure that the contacting components stay joined and the gross slip does not occur. Nevertheless, the small relative slip over parts of the contact interface, i.e. the micro-slip, contributes significantly to the vibration damping. In the high-fidelity analysis of practical bladed discs the macro-slip model cannot provide sufficient accuracy for the predictive analysis of the properties of the friction damping in the contact interfaces. In this article, numerical studies of micro-slip damping effects is performed using 2D and 3D models of blade root joints. Analysis of hysteresis loops is performed to assess the influence of modelling parameters: choice of reference points, mesh configurations and other physical parameters. The impact of physical parameters, such as the contact geometry, friction coefficient, contact stiffness and tangential and normal loading, on the friction damping are numerically examined. The numerical results demonstrate the possibilities of micro-slip prediction using finite element modelling and shows the micro-slip friction damping effects using simplified and realistic blade root models.

## Keywords

Blade root joints, micro-slip, macroslip, friction, vibrations, contact interface, hysteresis

## Introduction

In realistic bladed disks, the blade resonant vibrations can cause high cycle fatigue failures. Energy dissipation produced by damping devices with friction interfaces, such as

under platform damper[1, 2], blade roots[3- 5] and bolted joints, are effective way for the blade vibration level mitigation.

The reviews of current state-of-art for dynamic analyses of bladed disks with friction dampers can be found in Refs.[6-8]. The simplest model introduced for the friction damper analysis is a one-dimensional oscillator with Coulomb friction between blade and damper [9, 10]. Iwan suggested in Ref.[11] one-dimensional bilinear hysteretic restoring force model which was widely used to develop new friction models. Two-dimensional (2D) model with tangential motion and variable normal load was proposed for single harmonic balance methods in Refs.[12, 13]. This model was extended for the multi-harmonic balance method in Ref.[14]. Two-dimensional models with two-axial tangential motion and constant normal load were generated and developed in Refs.[15-17] for nonlinear dynamic analysis. By considering the variable normal load, a new friction model was then created in Refs.[18, 19] to simulate three-dimensional (3D) motion.

The macro-slip models allow the prediction of the friction forces at contact interface when there is the gross motion of one contact surface over another. There are attempts to generalize the macro-slip models to predict the dissipated energy over the whole contact interface using a relative displacement at a single contact point (see e.g. Ref[20]), but these models usually require large number of empirical or 'ad-hoc' parameters and generally have very small predictive capabilities. The mentioned macro-slip models could not give an exact description of the micro-slip effects with local slip-stick transition at the contact interfaces, they cannot allow for the complex geometric shapes of contact interfaces, realistic distributions of contact stresses, etc.

The microslip refers to the phenomenon when the relative tangential displacements occur over a part of the interface contacting area, while there are still parts of the contact interface where contacting surfaces are stuck, i.e. they do not slip. Therefore, there is no relative gross motion along tangential direction to the contact surface (Ref.[21]) and, due to large contact stiffness of the contact interface part the relative motion of contact interfaces is small, even when a small part of contact interface is stuck. Micro-slip behaviour at the friction contact interfaces contributes significantly to the structural damping and occurs in most of gas-turbine and other machinery structures. Micro-slip models are constructed often by using an array of macro-slip models with different model parameters allowing some of the macro-slip dampers from this array to slip earlier than the others (see Ref.[22]). The application of these models could be found in Refs.[23-27].

There are two major mechanisms (see Figure 1) of the dissipation energy at the contact interfaces which differ by the scales of the microslip friction energy dissipation. One mechanism is due to the micro-slip motion occurring at a portion of the contact interface area when the other part of the contact area stays in the suck state. This is large-scale micro-slip where the characteristic size of the microslip motion is related to the geometric size of the contact patch. Another mechanism considered by some researchers (see e.g. Ref[28]) are caused by microslip motion on much smaller scale when the slip, friction forces and energy dissipation occur between micro-asperities of rough surface contacts. This mechanism can provide vibration damping at contact interfaces even when

the whole contact surface area stays stuck and there is no relative motion between the pairing contact surfaces at any part of their contact area. The level of friction damping due to micro-asperity slip, plastic deformation of the microasperities, etc. is not fully negligible but expected to be significantly smaller than the damping due to slip at the part of the contact area. The importance of the accounting for micro-slip properties of the friction contact interfaces is demonstrated for structures with underplatform dampers in Ref.[29] Nevertheless, the possibility of prediction of the micro-slip friction damping assuming the friction contact between smooth surfaces has not been explored so far.

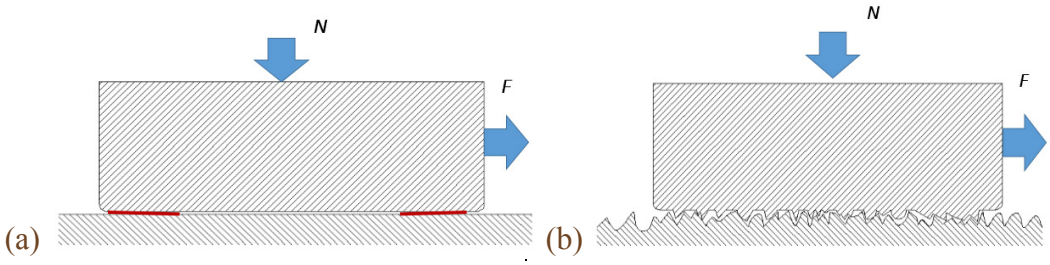


Figure 1. Two major damping mechanisms with microslip occurring: a) over part of interfaces; b) between micro-asperities of rough surfaces.

This paper considers the first from mentioned above mechanisms of microslip friction contacts: i.e. when the energy dissipation occurs due to slip at the part of the contact interface and can be modelled by the finite element contact elements on the scale much larger than the size of microasperities. The microasperities are not modelled individually but the surface roughness properties are included in the modelling by their statisticaly averaged characteristics that are measured experimentally, such as the friction coefficient, normal and tangential stiffness coefficients, (Refs.[16,30]) and used in the most of modern friction models. One of the goals of this paper is to demonstrate the possibility of modelling of the major microslip effects observed experimentally in measured hysteresis loops: e.g. smooth transition from full to partial stuck and then to gross slip of contacting interfaces. Different modelling aspects and the effects of friction interface parameters and on the hysteresis loops and energy dissipation at contact interfaces are studied.

Moreover, although there is a significant number of papers using macro-slip friction models and, sometimes, microslip models are also used in predictive analysis of dynamics, there have not been a systematic numerical analysis of microslip effects for friction modelling in blade-root joints.

This paper studies the influence of the contact interface parameters and blade root geometry in contact analysis of blade root joints on micro-slip transitions and hysteresis loops. Effects of friction modelling parameters and geometry of contact interfaces are explored including: friction coefficient, contact stiffness, variation of the contact interface geometry due to wear. The energy dissipation over the contact interfaces of a root joints during a vibration period and its dependency on the loading and root joint parameters are also investigated.

The first section of the paper introduces major approaches developed and applied here for the analysis of microslip. Then, in the second section, an investigation for relatively simple 2D contact models is performed. In third section 3D blade root models are analyzed, energy dissipation and the friction joint behavior is compared with 2D models and noticed differences are discussed.

## Methodology of the analysis

The equation for forced response analysis of a structure with nonlinear friction interfaces can be written in the following form

$$\boldsymbol{K}q(t) + \boldsymbol{C}\dot{q}(t) + \boldsymbol{M}\ddot{q}(t) + \boldsymbol{f}(q(t), \dot{q}(t)) = p(t) \quad (1)$$

where $q(t)$ is a vector of displacements for all degrees of freedom (DOFs) in the considered model; $\boldsymbol{K}$, $\boldsymbol{C}$ and $\boldsymbol{M}$ are stiffness, viscous damping and mass matrices accordingly; $\boldsymbol{f}(q(t))$ is a vector of nonlinear friction contact interface forces; and $p(t)$ is a vector of external excitation forces.

The microslip behavior at the friction contact interfaces is studied with a set of finite element (FE) models of a blade root joints: two dimensional (2D) and three-dimensional (3D) FE models. 2D models include: a block moving over another large block (see Figure 3a); and a simplified blade root model (see Figure 3b). 3D models include: a simplified blade root model (see Figure 16a) and a realistic blade root model (Figure 16b). To reduce the computational time the blade body is not modelled but the interaction of the blade body with the bladed root joint is modelled by the forces applied at the surface where the bladed root is attached to the blade.

The surface-to-surface contact interface elements are applied over the contact interfaces and the macroslip friction model is applied for each contact point. The multitude of contact elements allows capturing the effects of microslip: when some parts of the friction contact elements start slipping. The calculations are performed in ANSYS Workbench environment, and depending on the analyzed problems, two types of the contact elements are used: (i) for 2D contact problems a contact element CONTA172 is used, which is a 3-node surface-to-surface contact element; (ii) for 3D contact problems a contact element CONTA174 is used, which is a 3D 8-node surface-to-surface contact element.

The friction model in these contact elements is the modified Coulomb friction model, so that two contacting surfaces are subjected to elastic deformation without slip till the limiting friction stress values is reached and when slip occurs the friction stress level is equal to the limiting friction stress value. The limiting friction stress is determined as a product of the friction coefficient and the normal stresses at the contact point considered. Although the finite element code allows differentiate the dynamic and static friction coefficients, in our calculations the dependency of the friction coefficient on the relative velocity of slipping motion is neglected and the friction coefficient assumed constant over the time. The friction contact model uses two parameters of contact stiffness: (i) for interaction of the pairing contact surfaces along direction normal to the contact surface, $k_n$, and (ii) for interaction along direction tangential to the contact

surface, $k_t$. The physical cause of these stiffness coefficients is attributed usually (see e.g. Refs.13,19) due to roughness of the contact surfaces. The used finite elements allow to specify the values of each of the contact stiffness coefficients together with the friction coefficient value. Accordingly, in the calculation they are treated as physical stiffness coefficients and used to study the effects of the contact stiffness on the micro-slip behavior. In order to indicate ANSYS that the stiffness values are physical values and not penalty coefficients the values of the stiffness coefficients are provided with negative sign and with the absolute value equal to the stiffness coefficient magnitude.

There is a choice of three different solution methods for the nonlinear contact problems: (i) penalty method; (ii) Lagrange multiplier method and (iii) augmented Lagrange method. After extensive test calculations, the augmented Lagrange method has been chosen, since it combines the robustness of the solution search with the high accuracy of the obtained solution for the problems considered in this paper. The augmented Lagrange method uses the Lagrange multiplier component to get contact pressure from contact stiffness and other contact conditions at the last iterations while the robust convergence of the problem with contact constrained is ensured by using the penalty method contributions. Therefore, this method usually leads to well-conditioned matrices and is not very sensitive to the magnitude of the contact stiffness. In our calculations, the default Lagrange multiplier method parameters are used and the contact stiffness coefficients describing the physical properties of the rough surface contacts are provided in the input data for the friction contact finite elements.

The analysis is performed by the integration of the equation of motion in time domain using ANSYS implicit time domain solver. Owing to the fact that the natural frequencies of the considered friction joints are much higher than the vibration frequencies at which such joints operate in normal conditions the deformation of the joints is essentially quasi-static and the choice of the vibration frequency does not affect the results.

The parameters for the contact interfaces and the analyzed models can be separated into three main groups: (i) the analysis parameters to control the accuracy and speed of the calculation, (ii) the modeling parameters that define the nonlinear model and its excitation, and (iii) the friction interface parameters that describe the properties of the interfaces.

The analysis parameter set includes the choice of FE mesh used for modelling of contacting bodies, the quality of mesh used for the contact interface elements, the choice of the nonlinear contact equation solvers in ANSYS Workbench, and some others.

The modeling parameters include the geometry parameters and loads. The geometrical shape of the contact surface, contact angle effects (defined as the angle between the contact surface of the blade-disk joint and centrifugal loading direction) are considered here. Due to wear caused by friction forces at the contact interface the geometry of the contact surface can be subjected to small changes and the cases of the contact interfaces surfaces deviating from flat plane shape due to wear are also analyzed.

The combined action of static and dynamic loading is analyzed. The static loads in the rotating bladed disk are caused mostly by centrifugal forces, and the dynamic loads applied to the root joints simulate the forces applied to the blade root from a blade: they are caused in gas-turbine engines by bladed vibrations excited by varying in time aerodynamic pressure of the gas flow. The dynamic forces are assumed to be harmonically varying over time. In the considered analysis of root joints the blade vibration frequency is much lower that the frequencies of the blade root joint model and the frequency value chosen for the dynamic loading does not affect practically the contact interface behavior. The cases of uni-axial and bi-axial dynamic loading are considered and effects of different phase shift between these two loading direction: axial and tangential are studied.

The group of the friction interface parameters includes the friction coefficient, $\mu$, and the contact stiffness of friction interfaces due to the roughness of the contact surfaces: in normal direction $k_n$, and in tangential direction $k_t$. The friction contact parameters values depend generally on the material, surface finish, roughness, temperature, etc. Usually these values are determined from experimental measurements (e.g. see Ref.[31]) and the effect of these parameters on the micro-slip behavior of joints are explored in this paper.

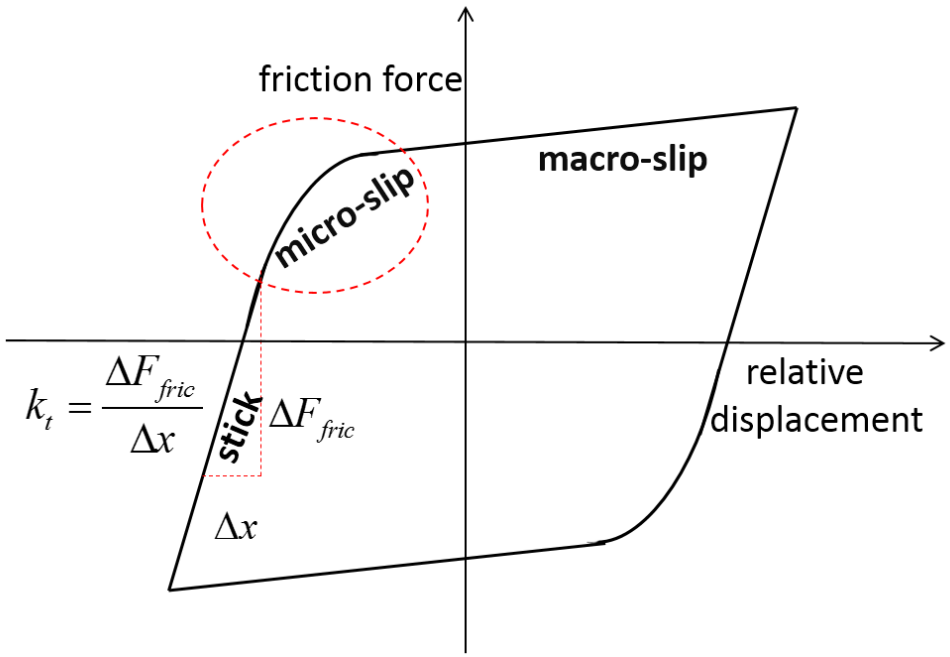


Figure 2. Example of hysteresis loop.

In Figure 2 a typical hysteresis loop obtained from experiments is shown. The friction coefficient expresses the relationship between normal pressure and friction shear stress. Contact stiffness gives the relationship between tangential force and relative displacement when a node is in stuck state. Micro-slip occurs during a process of transition between stick and gross slip. The relative displacement is defined as displacement difference between pairing contacting surfaces.

It should be noted that the conventional hysteresis loops were mostly plotted for contact interfaces with macroslip when a single point chosen at the contact interface can represent the relative displacement. For the joints subjected to microslip the relative displacement, $x^{\text{rel}}$ , can differ significantly at different points of the contact interface and, therefore, the hysteresis loops can differ significantly depending on the different choice the reference point used for the plotting the total friction force dependency on the relative displacement: $F(x^{\text{rel}})$. The analysis of effects of the reference point choice is explored in this paper.

The analysis is performed by calculating the deformation of FE models of the root joints and the friction and normal stresses at all time steps of the transient forced response analysis are calculated.

The nodal values of friction forces and displacements at the contact nodes are then exported from ANSYS to a specially created MATLAB code which processes the results in the form which is needed for the joint micro-slip analysis. Among the characteristics which are determined is the vector of total friction force calculated over the whole friction interface:

$$\boldsymbol{F}(t) = \sum_{j=1}^{N} \boldsymbol{f}_j(t) \qquad (2)$$

Where $N$ is the total number of contact interface nodes at the contact interface patch considered; $\boldsymbol{f}_j = \left\{ f_j^1, f_j^2 \right\}^T$ is the vector of nodal friction forces at $j$ -th node for 3D models, although for 2D model it becomes a scalar entity. The energy dissipated over a period of vibration, $W$ , is calculated in the form:

$$W = \int_0^T \left( \sum_{j=1}^{N} \boldsymbol{f}_j^T(t) \left[ \dot{\boldsymbol{u}}_j^{\text{contact}}(t) - \dot{\boldsymbol{u}}_j^{\text{target}}(t) \right] \right) dt \qquad (3)$$

Where $\dot{\boldsymbol{u}}_j^{\text{contact}}$ and $\dot{\boldsymbol{u}}_j^{\text{target}}$ are vectors of tangential velocities at the contact and target surfaces of the $j$ -th contact element. These velocities are determined for the tangential directions to the contact surface.

## Numerical studies for 2D models

In this section, two 2D models are explored: (i) a simple model (Figure 3a) and (ii) a simplified blade root model (SBRM) (Figure 3b). These models were built to investigate how the parameters (such as friction coefficient and contact stiffness) affect the micro-slip transition at the contact interface during small relative movement. The total number of quadratic plane stress finite elements in the 2D simple model is 1280 and the total number of finite element in 2D simplified blade root model is 4859. Surface-to-surface contact elements are applied in both cases and for 2D simple the number of interface

elements is 20 and 2D blade root model 28 contact elements are applied: 14 at each of two contact interfaces

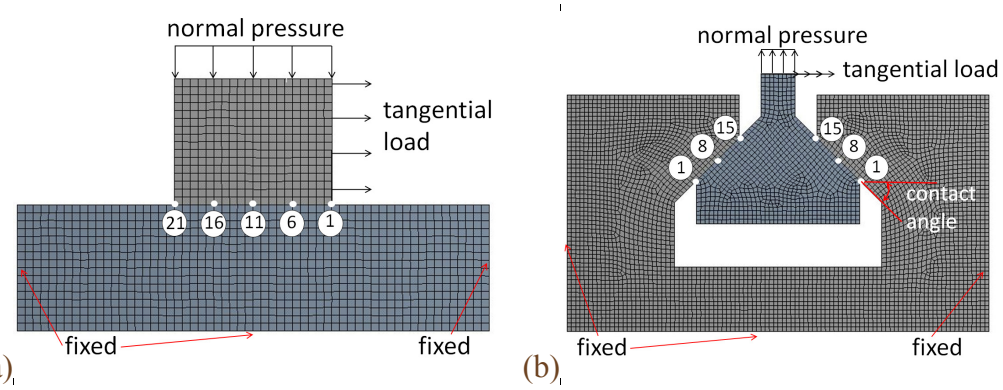


Figure 3. Finite element model a) the simple model; b) the simplified blade root model.

The simple model includes a block moving over flat elastic body. A constant uniformly distributed normal pressure is applied on the top of the block. Harmonically varying in time pressure, $P(t) = P_{\max} \sin(\omega t)$, is applied on the side of this block to invoke micro and macro slip at the friction contact interface (see Figure 3a). In this article, for most of calculations the vibration frequency used in calculation is assumed: $\omega = 10 rad/s$. Each vibration cycle is divided into 40 sub-steps – in order to obtain details of the hysteresis loops.

2D surface-to-surface friction contact elements are distributed uniformly over the friction contact interface to describe the nonlinear forces occurring between the two objects. The simplified blade root model shown in Figure 3b consists of two components, one is a part modelling the blade root and another one simulates a part of disk. These two parts are in contact at two contact surfaces and the normal pressure is applied at the top of the root: i.e. at the surface where the blade airfoil is attached. This normal pressure imitates the blade root loading caused by centrifugal forces. The so-called 'tangential' pressure is harmonically varying in time and this pressure imitates the forces applied to the root from the vibrating blade. External boundaries of the disk part are fixed as shown in Figure 3b.

## 2D simple model

The 2D simple model was studied first to explore the fundamental properties of micro-slip and to assess the influence of contact interface and loading parameters on micro-slip transition. The displacement control strategy is used in this model for most cases: to be able to model and calculate not only microslip but also macroslip and the rigid body motion of the block. The force control loading is applied here only for a case when the effect of the loading level is analysed. The displacement-controlled loading is applied in the form $x(t) = x_{\max} \sin(\omega t)$ , where $x_{\max}$ is the amplitude of the displacement applied imposed on all nodes of the vertical side of the block. The normal pressure is assumed: $N = 1$ MPa, and the amplitude of displacements is $x_{\max} = 5 \times 10^{-4} mm$. Normal contact

stiffness and tangential contact stiffness are $k_n = k_t = 10^5\ N/mm^3$ , and friction coefficient value is assumed: $\mu = 0.4$ . This set of parameters is adopted as a reference set and in the presented further analysis of parameters on the hysteresis loops one of these parameters was varied.

## Effect of Mesh Configuration

The mesh density of finite element model together with the number of contact elements affect computational efficiency, so the effects of mesh density used in the model is considered at first. Since computational efficiency and calculation accuracy are contradictory requirements, a correct balance between them should be chosen. The friction force was calculated for four different contact interface meshes: with 10, 20, 40 and 80 elements. The example of hysteresis loops with different number of contact elements over the contact interface are plotted in Figure 4. It is evident that results are very close for all cases and 20 contact element mesh is used in the following studies of this model. Displacement control is applied in this and further calculation, and contact node pair 11 in the middle is chosen as the reference node here.

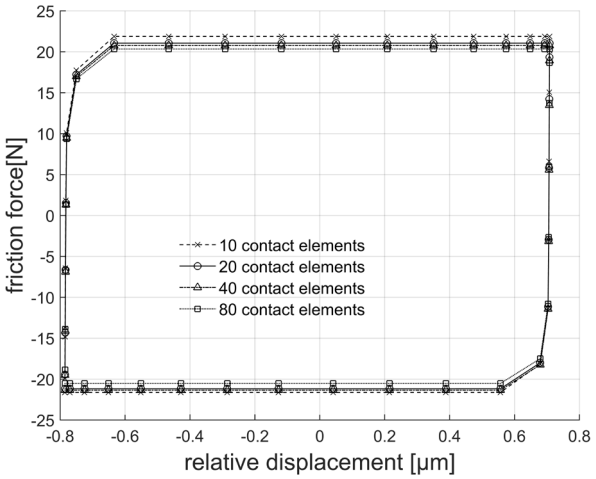


Figure 4. Hysteresis loop with different mesh configuration.

## Effect of tangential load

Tangential load is an important factor that determines the maximum relative displacement and the dissipation energy. The load control analysis is used for this case and the amplitude of the load is selected to achieve the convergence of numerical solution of the nonlinear contact problems for the cases. So, the amplitude of tangential load should not lead to fully developed rigid motion – which causes the loss of the convergence, nor be too small – when the microslip does not occur. Different tangential load with amplitude $P_{\max}$ are applied here: 0.7, 0.725 and 0.75 MPa. In Figure 5, the 6-th node is chosen as a reference point (see in Figure 3a) and the displacement of this node is plotted over the horizontal axis.

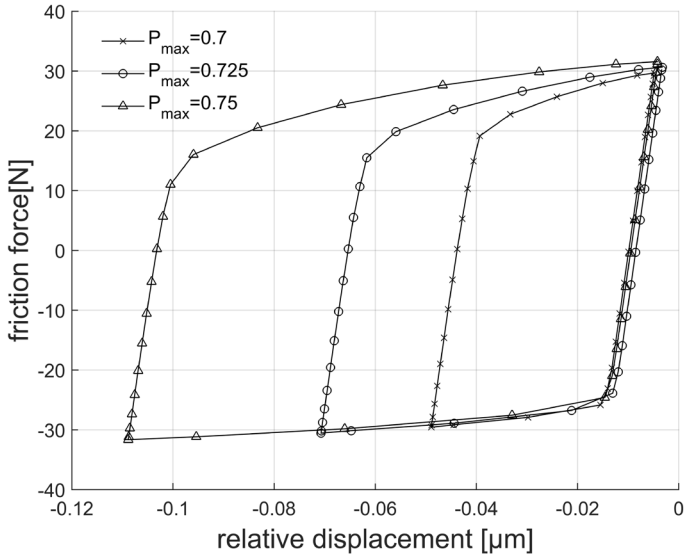


Figure 5. Hysteresis loop for different tangential load levels.

As expected the amplitude of relative displacement increases with the tangential load. Because of the action of the static loading by the normal pressure the relative displacements have a significant negative constant component and the hysteresis loops are shifted to the range of negative relative displacements. One can see that, when with the tangential load increases, the micro-slip occurs at a lower friction force level. Moreover, we can observe here a secondary slope in the hysteresis loop plot which occurs after the beginning of microslip: such slope is observed in many experimental measurements of the hysteresis loops (e.g. see Ref.[17]). Our analysis shows that the cause of this secondary slope is the residual stiffness of the part of the contact interface which is not involved in relative motion.

## Effect of the choice for the reference node

In the micro-slip model used here, the contact surface is modelled by multitude of contact elements and the relative motion is different for each contact node. The hysteresis loop shape is dependent on the choice of the node which is selected as a reference displacement in the hysteresis loop plots. In experimental measurements not all contact points are usually accessible and the effect of the choice of reference nodes is considered here to assess the effect of choice of the reference node and to choose such points for the analysis of the micro-slip properties of the contact interfaces. In Figure 6 the hysteresis loops are plotted for 5 different reference nodes chosen at the friction contact interface. The nodes examined here are shown in Figure 3a. For the node located far from the application of the tangential load (node 21) the relative displacement is smaller than the relative displacement at contact nodes (node 1) located close to the application. Accordingly, the micro-slip region in the hysteresis loop plotted here is much larger when node 1 is used as a reference point than for a case of node 21. The node located in the middle of the contact interface (node 11) can provide a representative information about elastic deformation, micro-slip transition and macro-slip in the analysis of friction contact problems and such choice is used in all following hysteresis loops and discussions.

Nevertheless, the fact that the shape of hysteresis loops is significantly dependent on the choice of the reference nodes need to be noticed and taken into consideration.

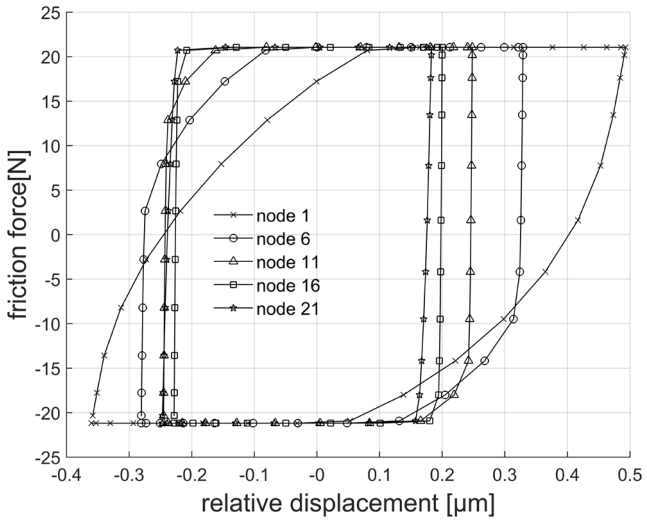


Figure 6. Hysteresis loop with different reference nodes

Figure 7 shows the status (stick or slip) for all contact elements during 3 cycles of loading. We can observe that the elements located closer to the applied load are in the slip state during larger part of the loading cycle, while elements located far from the load application stay in the stick state the most time of the loading cycle. Node pair 1 is located at the point where the load is applied, and node pair 21 is at the free end (see Fig.1a

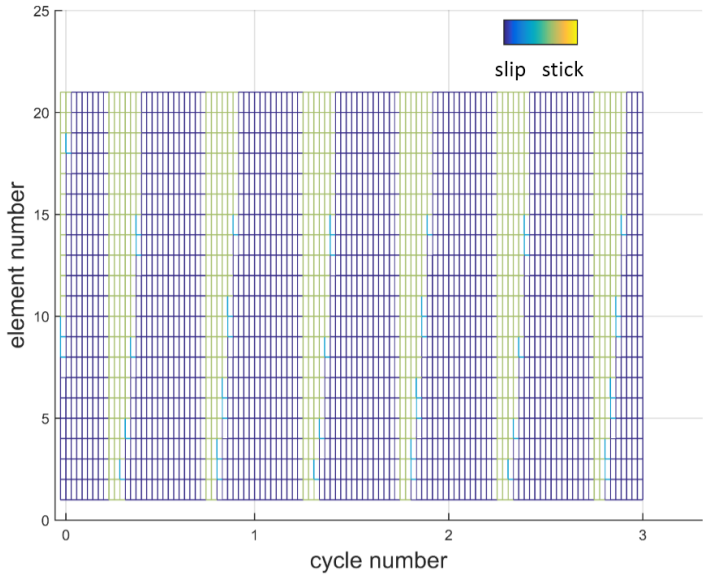


Figure 7. Status of contact elements

## Effect of contact parameters

As stated in the introduction, the commonly considered parameters in friction problems are: friction coefficient, the normal and tangential contact stiffness. In this section the effect of these parameters on the hysteresis loops is analyzed. Figure 8a shows that the hysteresis loops with different normal contact stiffness are very similar, although they are not coinciding exactly and the normal contact stiffness has little effect on the start of micro-slip transition here.

The effects of the tangential contact stiffness are shown in Figure 8b. As expected, the slope of the curve in the hysteresis loop region corresponding to stick changes with the changes of the tangential contact stiffness. However, for smaller values of the contact stiffness this slope changes almost proportionally to the stiffness change, but for sufficiently large values of the tangential stiffness the effects of their variation becomes negligent since the elasticity of the bulk material becomes dominant for high values of the contact stiffness. The micro-slip region has the tendency to decrease with the increase of the tangential stiffness. This is due to the fact that when the tangential stiffness increases, the block starts to move as a rigid body earlier since all contact nodes reaches their limiting friction stress level earlier.

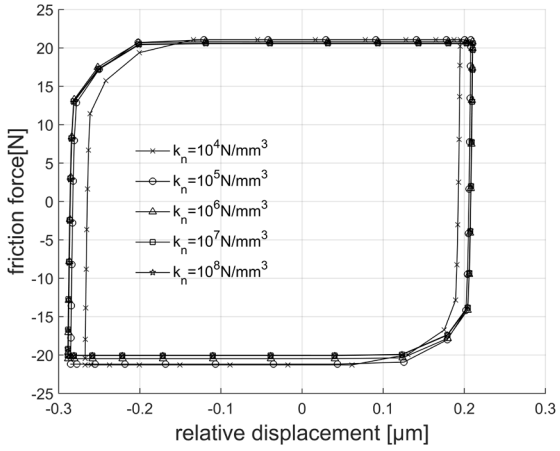


(a)

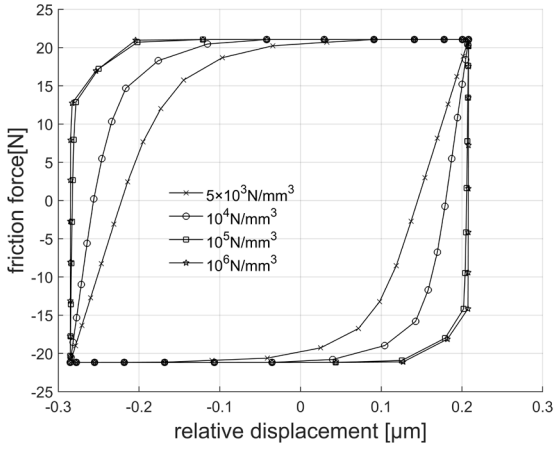


(b)

Figure 8. Hysteresis loop with stiffness variation a) normal b) tangential.

In Figure 9 the effects of friction coefficient and normal pressure are shown. In Figure 9a, the normal pressure is set to 1 MPa, and friction coefficient value is varied, while in Figure 9b, the friction coefficient is set to 0.4, and the calculations are performed with different normal pressures. These two parameters defines the limiting friction force level at each node of the friction contact interface: $F_{\text{limit}} = \mu N$ . The hysteresis loops have the similar trends for these two parameters, although they do not coincide exactly. The amplitude of relative displacement decreases with the increase of friction coefficient and normal pressure, while the friction force increases. The micro-slip region of the hysteresis loops increases with the increase of these two parameters and the macroslip region decreases significantly. The hysteresis loop is affected by the normal pressure and friction coefficient, but the effects are not exactly the same since the normal pressure causes different elastic deformations and stress fields in the model and those have an additional effect on the relative displacement.

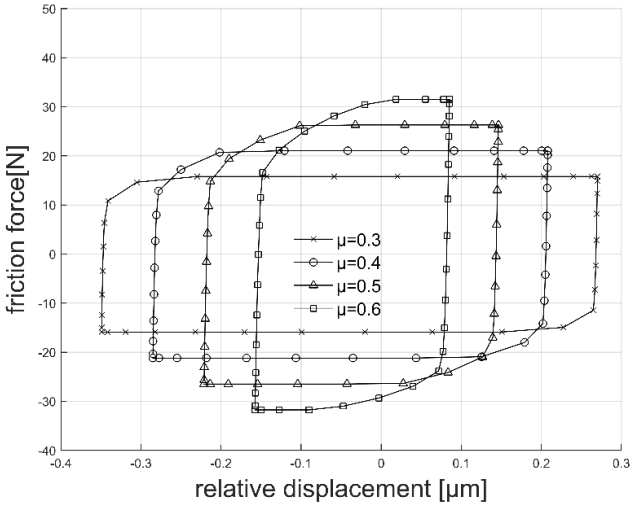


(a)

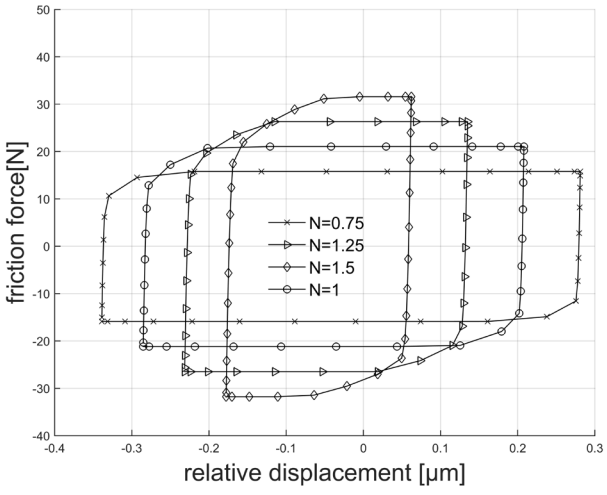


(b)

Figure 9. Hysteresis loop with a) friction coefficient and b) normal pressure

## Contact surfaces considering wear

The contact surfaces in gas-turbine engines operating sufficiently long time can lose their initially flat shape due to friction-induced wear. To explore the effects of small geometry variation in geometry of contact surfaces two kinds of surface shapes are created and shown in Figure 10. They are: (i) a case when upper surface is convex and lower is flat and (ii) a case when lower surface is concave and upper surface is flat. The cases of contact length values 10, 20, 30, 40 mm are studied (marked in the Figures. 11a and 11b as 'L'). Middle node 11 is the reference node chosen for the case when the upper surface is convex, because the middle of the contact surface is always in contact. For the same reason, the nodes (node 1 and 21) in both ends are selected for the case when the lower surface is concave.

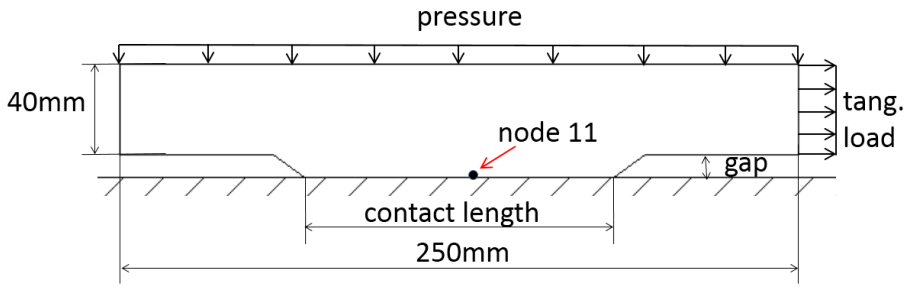


(a)

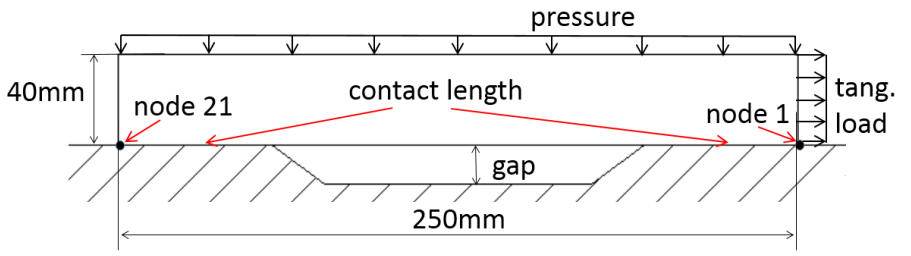


(b)

Figure 10. Schemes of different contact geometries: a) the model of the convex contact surface geometry; b) the model of the concave contact surface geometry.

The effect of the contact patch length for a case of convex upper surface is illustrated in Figure 11a. It is evident that with the increase of the contact length, the amplitude of relative displacement and the micro-slip region increases but the friction force decreases. This effect is opposite to that shown in Figure 9, when the normal pressure was varied. It is because when normal pressure is kept constant and contact length increases, the normal stress distributed in the contact surface reduces, as a result the microslip occurs over larger area. It should be noted here that the normal stress at the contact interface affects the interaction at the contact surface in reality rather than the normal load applied to the block. The micro-slip region increases with the increase of the contact length.

The results obtained for the case of concave lower surface are shown in Figure 11b. The hysteresis loops are plotted for two choices of the reference point: node 1 and node 21 (see Figure 10b). It can be observed, the micro- slip region increases when with

the contact length increase. The shape of the hysteresis loop is much affected by the choice of the reference point.

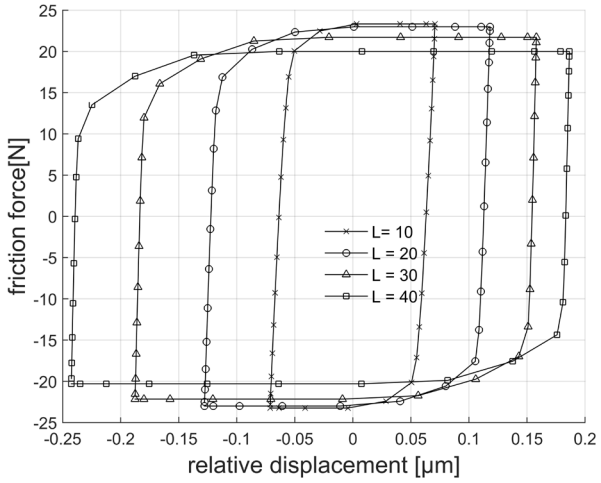


(a)

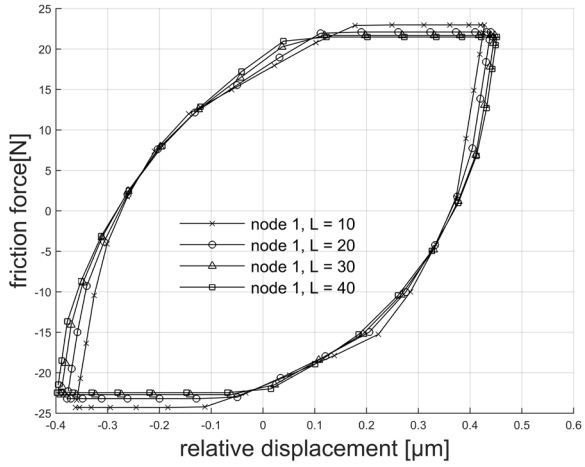


(b)

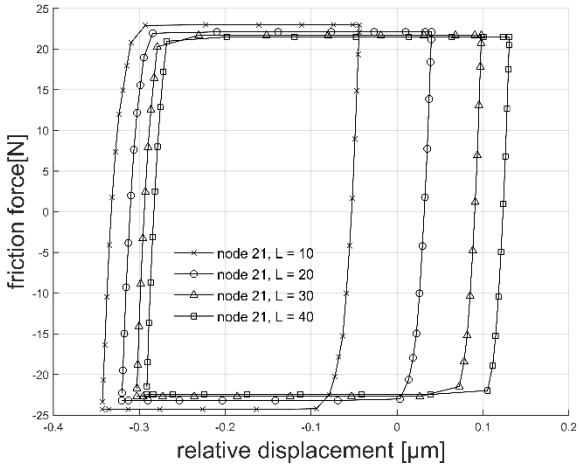


(c)

Figure 11. Hysteresis loops for different contact lengths a) the convex upper surface case b) lower surface is concave for reference node 1 and c) for reference node 21

## 2D simplified blade root model

2D simplified blade root model (SBRM) shown in Figure 3b is analyzed and the following contact interface parameters are used in the calculations: $k_n = 10^6\, N/mm^3$; $k_t = 10^4\, N/mm^3$ ; and $\mu = 0.4$ . Similar to the model analysed in the previous section (see Fig.4) the effect of the number of friction contact element has been studied for SBRM. It was found that more than 14 elements at each of the two contact surfaces on both sides of the root model could provide results when the hysteresis loop is not changed by the increase of the contact element number. Therefore, 28 contact elements are used in this calculation: 14 contact elements at each side.

The force controlled loading is considered here. The normal pressure is assumed to be 19MPa and the tangential pressure is harmonically varying: $P(t) = P_{\max} \sin(\omega t)$. These loads are applied as it is shown in Figure 3b. The major difference of the SBRM from the simple model considered before is that the SBRM has two contact surfaces and these surfaces are inclined with the respect to the applied normal loading. Moreover, the constraints from two contact surfaces prevent the motion of the blade root as rigid body and the force control strategy can be applied here. The contact interface nodes at two contact surfaces are numbered in similar way on left and right contact interfaces as it is shown in Figure 3b.

The distribution of normal and shear stress lie on the contact surface after the application of static normal load for left and right sides of the contact surfaces are shown in Figure 12. The distribution of these two stress is almost symmetric, except that shear stress has an opposite direction for two sides. The stress levels at contact nodes located further from the load application is significantly larger, moreover, the stress concentration effect is observed at the ends of the both contact surfaces.

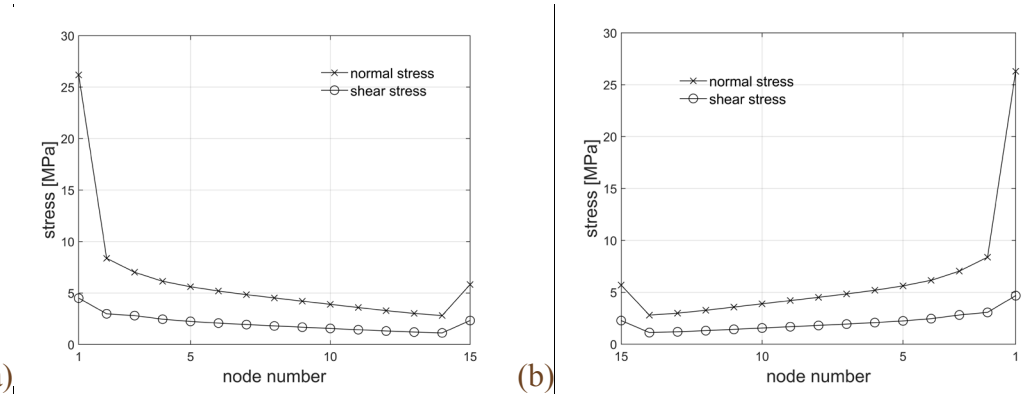


Figure 12. Normal and tangential stress distribution on contact surfaces for a) left side and b) right side.

The effects of the tangential stiffness on hysteresis loops are illustrated in Figure 13. The friction forces are calculated separately for left and right contact interface and the nodes in the middle of the both contact patches (node 8 in Figure 3b) are used as the reference point. It is evident large regions of the microslip in the hysteresis loops.

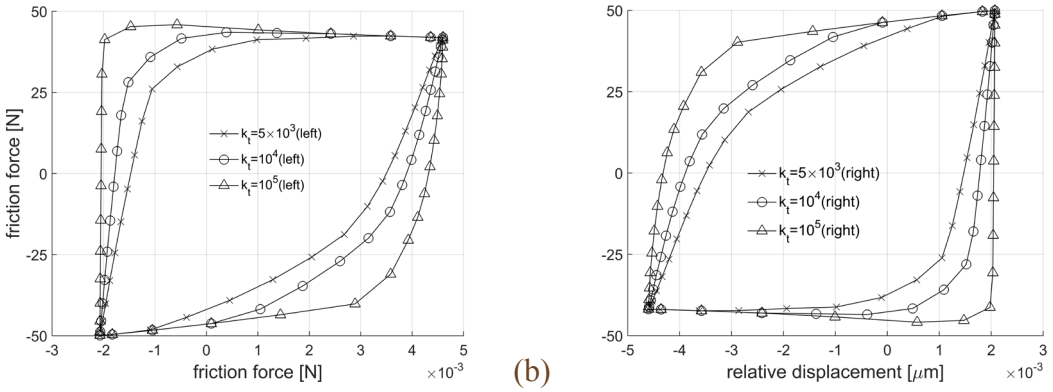


(a) (b)

Figure 13. Hysteresis loop with tangential stiffness variation for a) left side and b) right side.

## Effect of contact angle

The contact angle is a new parameter in this model. The contact surfaces in realistic blade roots have also contact surfaces inclined to the blade axis and the effect of the inclination angle is necessary to consider. 2D simplified blade root models with contact angle 40°, 45°, 50° were created with the contact length kept in these models the same. The results of calculations are shown in Figure 14. Due to root symmetry the shapes of the hysteresis loops for left and right sides of the blade root are very similar and differ mostly by the phase of relative motion. One can see that the amplitude of friction force increases with the contact angle increase, while the amplitude of the relative displacement and the micro-slip region size decreases.

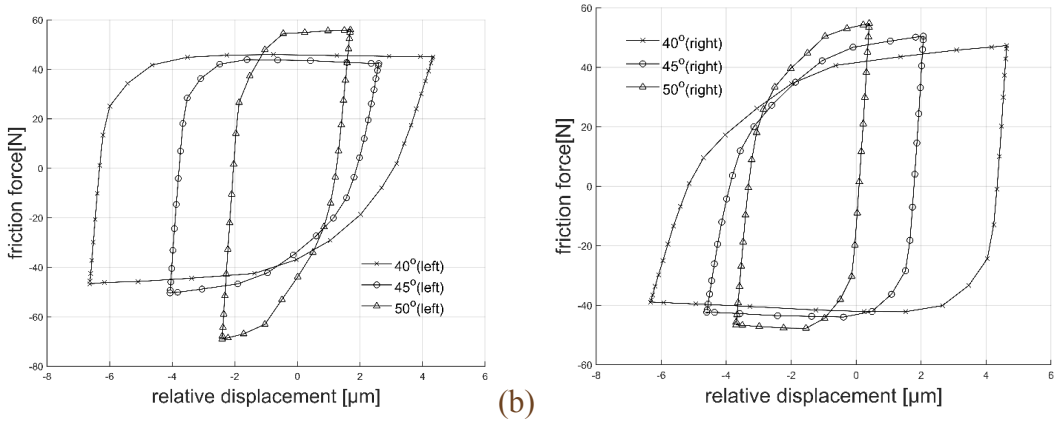


(a) (b)

Figure 14. Hysteresis loop with contact angle variation for a) left side and b) right side.

The energy dissipated at both contact patches over one period is plotted in Figure 15 as a function of the contact angle. It can be seen that the dissipated energy is very dependent on the angle and change the inclination angle by 10° can change the amount of

dissipated energy more than 200%. The increase of the angle decreases the energy dissipation, which can be explained by the reduction of the contact areas subjected to the slip and, therefore, by the reduction of the energy dissipated by friction.

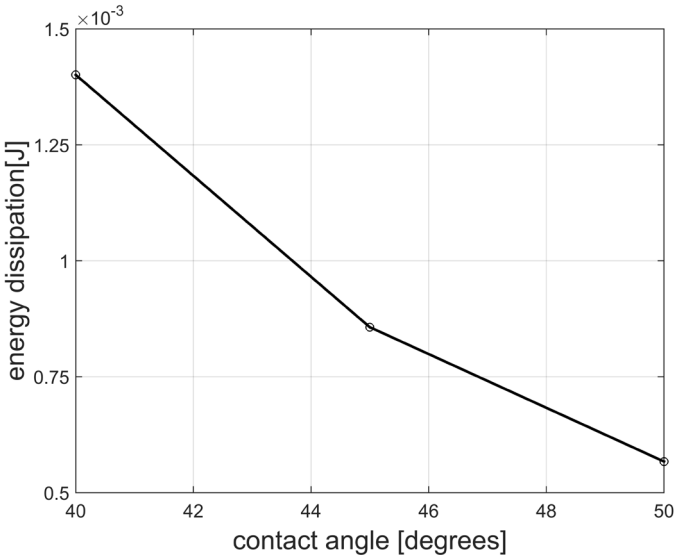


Figure 15 Figure with energy dissipation.

# Numerical studies for 3D models

3D models investigated here are blade root models. A model corresponding to 2D SBRM is analyzed here first, and then, a model created by cutting a root joint from a realistic bladed disc is studied. These two 3D models are named as a simplified blade root model (3D SBRM) and a realistic blade root model (RBRM). Their finite element models are shown in Figure 16. 3D SBRM contains 15184 quadratic solid elements together with 78 3D surface-to-surface contact elements. RBRM contains 21084 quadratic solid elements with 2128 contact elements distributed over blade root contact areas.

In 3D SBRM the contact elements are distributed over two contact surfaces to simulate the interaction between blade and disc, which is similar to that in 2D SBRM.

For the realistic blade root model, the blade root was separated from the blade by cutting it below the turbine blade platform. This is done to save the computation time by exclusion of the blade body DOFs form the time integration process.

For these models, the force control is applied and the normal load and the tangential load are distributed uniformly on the top of the blade root in the form of pressure and traction stresses (called further as tangential pressure) respectively. The tangential load in direction 1 is harmonically varying in time similar to all considered earlier cases of analysis of 2D models. The disk parts used to model the disks are fixed at their outer surfaces (see Figure 16). In all these models, the normal and tangential contact stiffness are $k_n = k_t = 10^5 N/mm^3$, and the friction coefficient is $\mu = 0.4$.

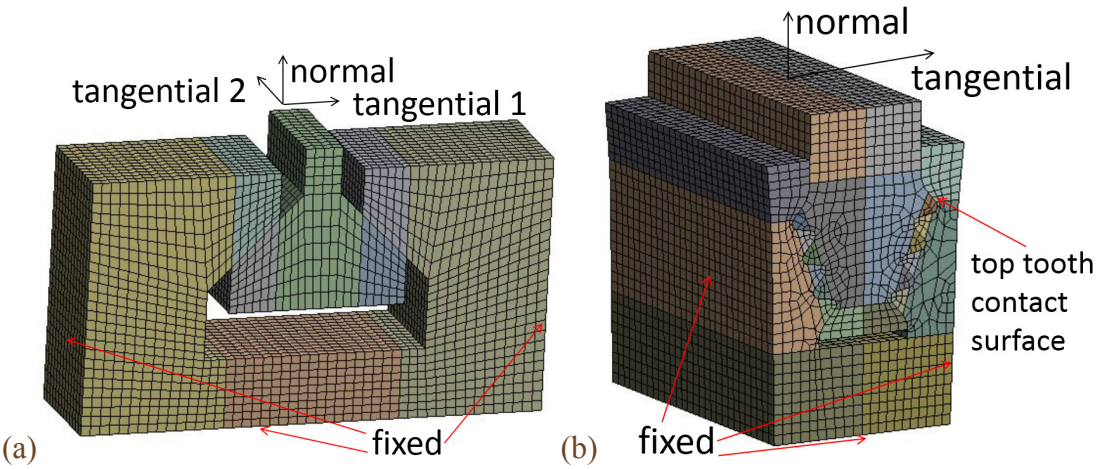


Figure 16. Finite element model a) the simplified blade root model b) the realistic blade root model.

## 3D simplified blade root model

For calculations of 3D SBRM, the normal pressure is assumed to be 50MPa and the amplitude of tangential pressure is 21MPa. The effects of contact interface parameters on the friction contact behavior calculated for this model are very similar to what was obtained for 2D SBRM, except for the normal contact stiffness. Only the effect of normal contact stiffness is discussed below for this model.

### Effect of normal stiffness

Figure 17 shows how the hysteresis loops for different the normal contact stiffness values plotted for the right contact interface and with the reference displacement chosen is the middle point of the right contact surface. Two differences can be found in this figure comparing with results for 2D simple model (Figure 8). The first is that for 2D simple model, the hysteresis loops for different normal contact stiffness are nearly coinciding, while for 3D model the increase of normal contact stiffness reduces significantly the amplitude of relative displacements and the micro-slip region increases. The second is that because of application of the static loading, which causes the initial shift of the pairing contact nodes, the relative displacement for the right contact patch is positive most of the time. The hysteresis loops for the left patch of this model were similar to that for right patch, in the way as demonstrated above for 2D SBRM.

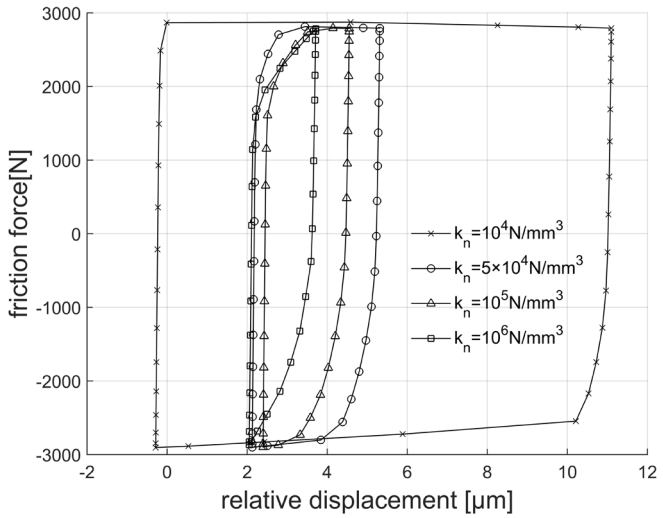


Figure 17. Hysteresis loop with normal stiffness variation: right contact patch.

## Energy dissipation

The energy dissipation is an important characteristic since it defines the damping of the resonance vibration in friction joints. The results of energy dissipation calculations obtained for variation of different parameters are shown in Figures 18.

With the increase of normal load, the energy dissipated for one cycle increases at the beginning due to the increase of the friction forces at the parts of the surfaces subjected to slip (Figure 18a). Then after reaching the maximum the dissipation energy starts to decrease, which is due to decrease of the area subjected to the microslip. Further normal pressure increase could almost completely suppress the micro-slip friction energy dissipation. Similar dependence and the same mechanism of the influence on the dissipation energy is observed for friction coefficient variation (Figure 18a). The increase of the tangential stiffness facilities the beginning of microslip over larger areas and the dissipation energy increases with its increase, while the effect of the normal stiffness increase is opposite (Figure 18b). The increase of the tangential load increases the dissipation (Figure 18c) due to the increase of the microslip area and increase of the relative motion at the contacting interface.

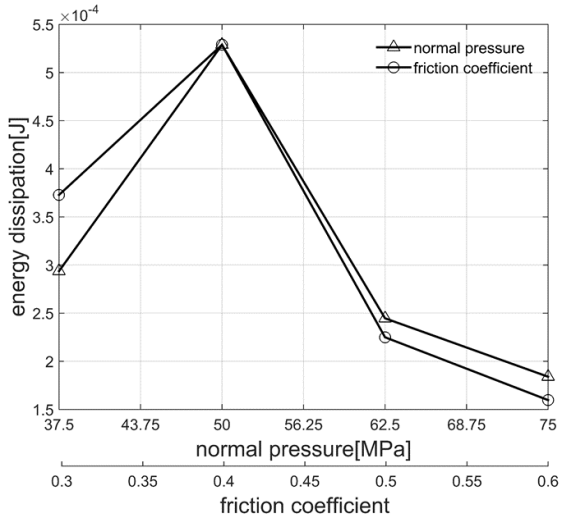


(a)

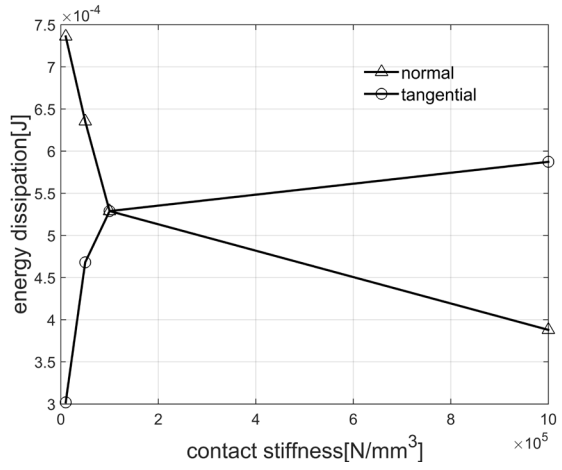


(b)

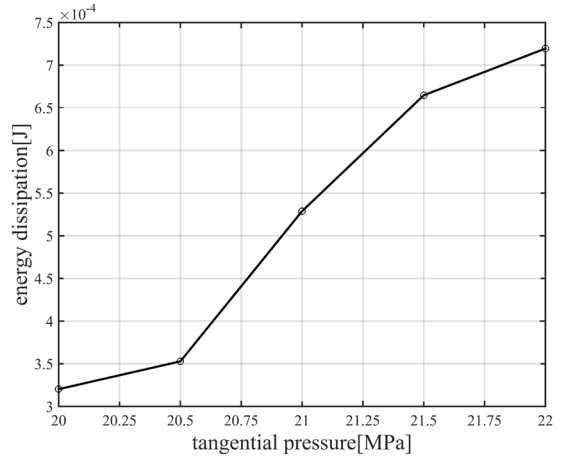


(c)

Figure 18. Energy dissipation a) with normal load and friction coefficient variation b) with contact stiffness variation c) with tangential load variation under load control.

## Effect of phase difference between two tangential loads

The tangential loads applied to blade roots in bladed disks can be generally represented by two components acting along two perpendicular directions within the plane where the blade root interacts with the blade. Moreover, some phase difference between these two components of the tangential load can exist. In order to study whether the phase difference has influence on micro-slip transition, two components of the tangential load are applied (see Figure 16a):

$$P_1(t) = P^1_{\max} \sin \omega t \;\; ; \;\; P_2(t) = P^2_{\max} \sin(\omega t - \theta) \quad (4)$$

Where $P^1_{\max}$ and $P^2_{\max}$ are amplitudes of the tangential load components and $\theta$ is the phase difference between them.

The variation of the contact status at contact interface over one loading cycle is shown in Figure 19 for time instants equally distributed over this cycle. Both slipping and stuck contact nodes coexist in the contact surface since the micro-slip occurs here.

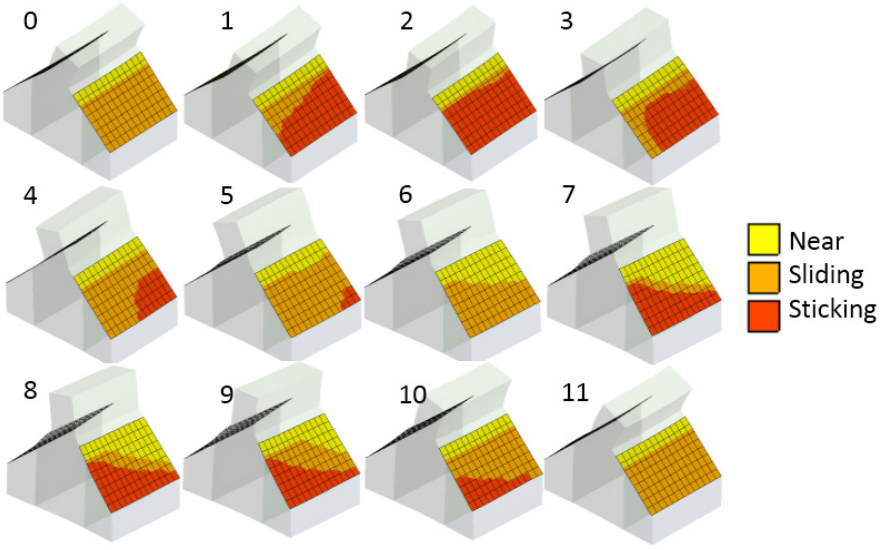


Figure 19. Contact status changes over a cycle.

The dependency of the hysteresis loops on the phase shift between $P^1$ and $P^2$ is shown in Figure 20 where the friction force is plotted for the right side patch of the root joint and the direction of this force is 1, i.e. the component of the friction force which is dominant for the considered loading. When the phase shift increases from 0 to 90°, the amplitude of relative displacement have a tendency to decrease. We can see also a phenomenon which was not observed for cases considered before: the sharp corners corresponding to stuck state on the hysteresis loop are smoothened and start to look more like a circle with the phase shift increase.

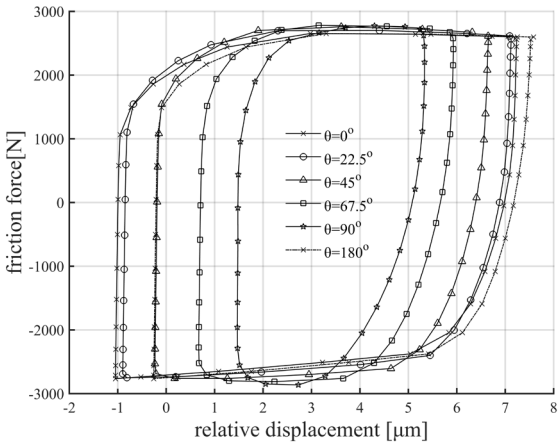


Figure 20. Hysteresis loop with phase difference variation.

## 3D realistic blade root model

In the RBRM, the contact surface is complex and comprises four fir-tree teeth located. 20MPa normal pressure with 10MPa amplitude of harmonically varying tangential pressure are applied on the top of the modified blade root (see Figure 16b).

### Variation of the friction stresses

The friction stresses over the contact surfaces of RBRM are shown for different time steps over loading in Figure 21.

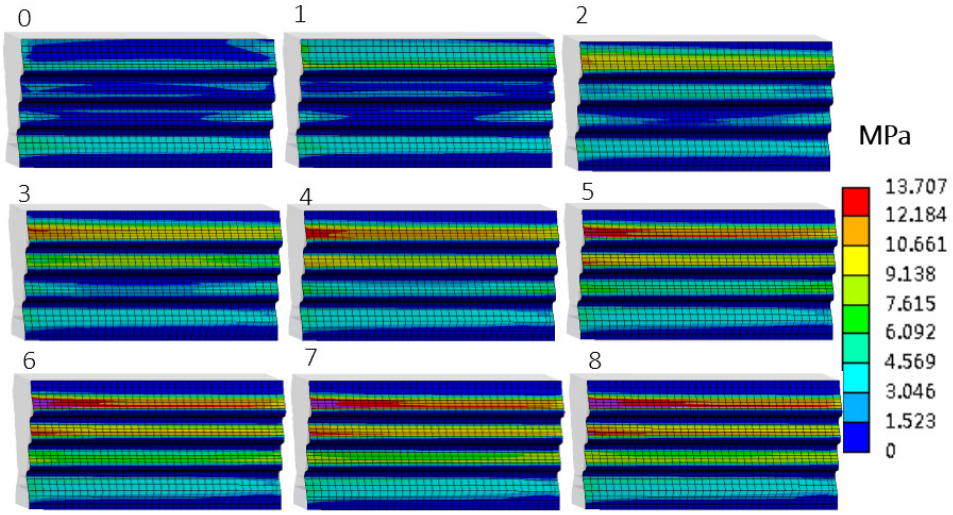


Figure 21. Friction stress distribution changes with time.

One can see that the maximum of the friction stress occurs at the top tooth of the fir-tree blade root. Therefore, this contact surface of this tooth is selected as the contact surface for plotting the contact interface hysteresis loops. The middle node of this surface is chosen as the reference node for investigation of the microslip property in the realistic blade root joint.

## Effect of contact parameters

The effect of amplitude of the tangential loading is shown in Figure 22a. It is evident that micro-slip occurs during the loading and unloading process and the increase of the loading makes the micro-slip effects more noticeable. The shape of the hysteresis is different for the loading and unloading. The relatively small increase of the tangential loading increases significantly the relative displacement, the hysteresis loop area and, accordingly, the dissipated energy on the blade root tooth considered here.

The effect of tangential contact stiffness variation on the hysteresis loop is displayed in Figure 22b. We can see that the tangential stiffness affect significantly the microslip region of the hysteresis. With the stiffness increase the microslip starts with much smaller levels of the relative displacements. The slope of the stick hysteresis loop region is proportional to the tangential stiffness of the contact surface.

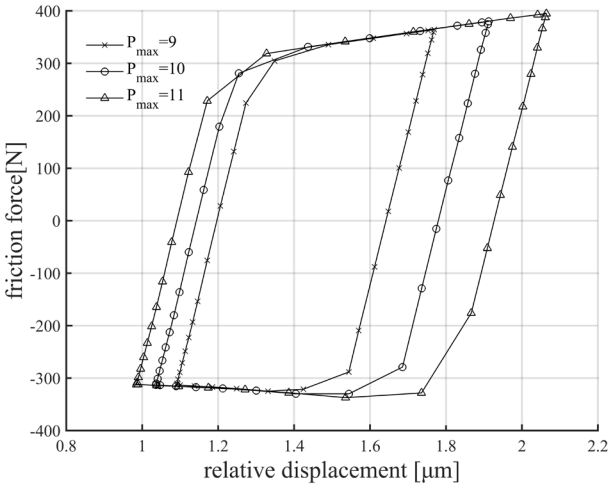


(a)

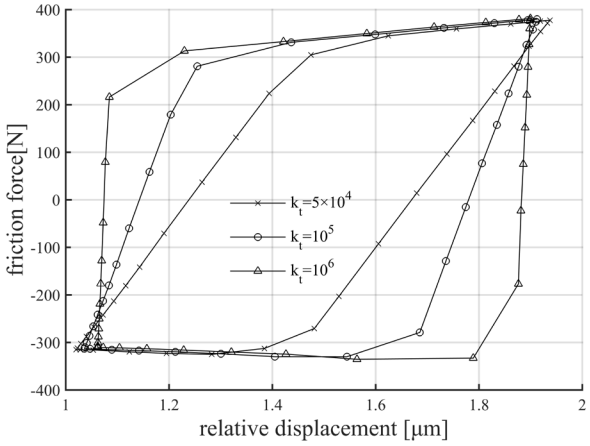


(b)

Figure 22. Hysteresis loop a) with tangential load variation b) with tangential contact stiffness variation.

The effect of the friction coefficient and normal load on the hysteresis loops is shown in Figure 23. It should be noted that the variation of the friction coefficient and normal load changes the hysteresis loops differently, although both reduces the level of friction force when the micro-slip starts

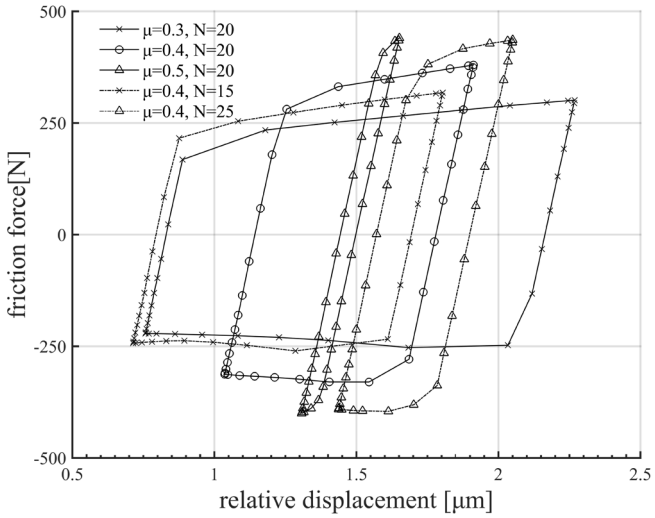


Figure 23. Hysteresis loops for friction coefficient and normal load variation.

# CONCLUSIONS

Numerical studies of the micro-slip damping effects in blade root joints have been carried out. Two dimensional and three-dimensional simplified and realistic models of blade-root joints have been considered. The effects of contact interface parameters, contact interface geometry and different loading conditions have been comprehensively studied. The numerical results give a useful insight in the micro-slip friction damping effects and their role in predicting the vibration levels of blade root joints.

Effects of the variation of contact area which can be caused by the wear of rubbing surfaces on the hysteresis loops have been modelled and studied. It is shown that the contact area size can affect significantly the hysteresis loop shape, including the micro-slip regions.

Using 3D blade root models the effects of normal and tangential load levels, friction coefficient, tangential and normal stiffness coefficients on the energy dissipated over a cycle of periodic loading have been explored.

It is shown that the angle of inclination of the contact surfaces in blade rood teeth can significantly affect the friction damping properties of the root joint. For the considered examples the increase of the angle decreased the energy dissipation.

# Acknowledgement

This work was supported in part by the National Natural Science Foundation of China (Project No. 51175244, No. 11372128), and NSAF (Project No.U1730129), the Natural Science Foundation of Jiangsu Province (No. BK20161485) and Jiangsu Province Key Laboratory of Aerospace Power System (No. NJ20160019). The supports by the Collaborative Innovation Center of Advanced Aero-Engine, the Key Laboratory of Aero-engine Thermal Environment and Structure, Ministry of Industry and Information Technology are also gratefully acknowledged.

# Reference

1. Petrov EP. Explicit finite element models of friction dampers in forced response analysis of bladed disks. J of Eng for Gas Turbines & Power 2008; 130(2): 277-285, 200.

2. Firrone CM, Zucca S and Gola MM. The effect of underplatform dampers on the forced response of bladed disks by a coupled static/dynamic harmonic balance method. Int J of Non-Linear Mechanics 2011; 46(2): 363-375.

3. Petrov EP and Ewins DJ. Effects of damping and varying contact area at blade-disc joints in forced response analysis of bladed disc assemblies. J of Turbomachinery 2005; 128: 495-504.

4. Charleux D, et al. Numerical and experimental study of friction damping blade attachments of rotating bladed disks. Int. J. of Rotating Mach 2006: 1–13.

5. Zucca S, Firrone CM, and Gola MM. Numerical assessment of friction damping at turbine blade root joints by simultaneous calculation of the static and dynamic contact loads, Nonlinear Dynamics 2012, 67(3): 1943-1955.

6. Griffin JH. A review of friction damping of turbine blade vibration. Int J of Turbo & Jet Engines 1990; 7(3-4): 297-308.

7. Rizvi A, Smith CW and Rajasekaran R, et al. Dynamics of dry friction damping in gas turbines: Literature survey. J of Vibration and Control 2014; 22(1):296-305.

8. Krack M, Salles L, and Thouverez F. Vibration Prediction of Bladed Disks Coupled by Friction Joints. Archives of Computational Methods in Eng 2017, 24(3):589-636.

9. Griffin JH. Friction damping of resonant stresses in gas turbine engine airfoils. J of Eng for Power 1980; 102: 329–333.

10. Cameron TM, et al. An integrated approach for friction damper design. J of Vibr And Acoust 1990; 112: 175-182.

11. Iwan WD. The dynamic response of bilinear hysteretic systems. PhD thesis, California Institute of Technology, 1961.

12. Yang BD and Menq CH. Characterization of contact kinematics and application to the design of wedge dampers in turbomachinery blading: Part 1—Stick-Slip Contact Kinematics. J of Eng for Gas Turbines & Power 1997; 120(2): 410-417.

13. Yang BD and Menq CH. Characterization of con-tact kinematics and application to the design of wedge dampers in turbomachinery blading: Part 2—Prediction of forced response and experimental verification. J of Eng for Gas Turbines & Power 1997; 120(2): 418.

14. Petrov, EP, Explicit finite element models of friction dampers in forced response analysis of bladed disks. J of Eng for Gas Turbines & Power, 2008, 130(2):277-285.

15. Sanliturk KY and Ewins DJ. Modelling two-dimensional friction contact and its application using harmonic balance method. J of Sound & Vibration 1996; 193(2): 511-523.

16. Menq CH and Yang BD. Non-linear spring resistance and friction damping of frictional constraint having two-dimensional motion. J of Sound & Vibration 1998; 217(1): 127-143.

17. Schwingshackl CW, Petrov EP, and Ewins DJ. Measured and estimated friction interface parameters in a nonlinear dynamic analysis. Mechanical Systems & Signal Processing 2012; 28(2): 574–584.

18. Yang BD. and Menq CH. Characterization of 3D contact kinematics and prediction of resonant response of structures having 3D frictional constraint. J of Sound & Vibration 1998; 217(5): 909-925.

19. Schwingshackl CW, Petrov EP and Ewins DJ. Effects of contact interface parameters on vibration of turbine bladed disks with underplatform dampers. J of Eng for Gas Turbines & Power 2012; 134: 032507/1-032507/8.

20. Menq CH, Bielak J and Griffin JH. The influence of microslip on vibratory response, part I: A new microslip model. J of Sound & Vibration 1986; 107(2): 279-293.

21. Crook P and Farmer HN. Friction, lubrication, and wear technology. Materials Handbook, ASM Int, Materials Park, OH, 1992; 18: 758–65.

22. Sanliturk KY, Ewins DJ and Stanbridge AB. Underplatform dampers for turbine blades: Theoretical modeling, analysis, and comparison with experimental data. J of Eng for Gas Turbines and Power 2001; 123: 919–929.

23. Sextro, W. The calculation of the forced response of shrouded blades with friction contacts and its experimental verification. In: Proceedings of 2nd European Nonlinear Oscillation Conference, Prague, Czech Republic, 9–13 September 1996.

24. Petrov EP and Ewins DJ. Analytical formulation of friction interface elements for analysis of nonlinear multi-harmonic vibrations of bladed discs. J of Turbomachinery 2003; 125(2): 364-371.

25. Petrov EP and Ewins DJ. Advanced modeling of underplatform friction dampers for analysis of bladed disk vibration. J of Turbomachinery 2007; 129(1): 143-150.

26. Schwingshackl CW and Petrov EP. Modelling of flange joints for the nonlinear dynamic analysis of gas turbine engine casings. J Eng Gas Turbine Power 2012; 134(12): 122504/1 - 122504/9.

27. Krack M, et al. Reliability optimization of friction-damped systems using nonlinear modes. J of Sound & Vibration 2014; 333(13): 2699-2712.

28 Tworzydlo WW., Cecot W, Oden JT and Yew CH. Computational micro- and macroscopic models of contact and friction: formulation, approach and applications. Wear 1998, 220: 113–140

29. Gastaldi C, and Gola MM. On the relevance of a microslip contact model for under-platform dampers. International Journal of Mechanical Sciences 2016, 115: 145-156.

30. Schwingshackl CW, Petrov EP, Ewins DJ. Validation of test rig measurements and prediction tools for friction interface modelling. J of Turbomachinery 2010: 1015-1024.

31. Schwingshackl CW and Natoli A. Explicit modelling of microslip behaviour in dry friction contact. In: 34th IMAC Conference and Exposition on Structural Dynamics, Orlando, Florida, USA, 25-28 January 2016, Volume 4, 265-272. Cham: Springer.